Unveiling the molecular mechanisms of the type IX secretion system's response regulator: Structural and functional insights

Anshu Saran [ID][a,b], Hey-Min Kim[c], Ireland Manning[d], Mark A. Hancock [ID][b,e], Claus Schmitz [ID][f], Mariusz Madej [ID][g], Jan Potempa [ID][g,h], Maria Sola [ID][f], Jean-François Trempe [ID][b,e], Yongtao Zhu [ID][d,i], Mary Ellen Davey [ID][c] and Natalie Zeytuni [ID][a,b,*]

[a]Department of Anatomy and Cell Biology, McGill University, 3640 Rue University, Montreal, QC H3A 0C7, Canada
[b]Centre de Recherche en Biologie Structurale (CRBS), McGill University, 3649 Promenade Sir William Olser, Montreal, QC H3G 0B1, Canada
[c]Department of Microbiology, The Forsyth Institute, 245 First St, Cambridge, MA 02142, USA
[d]Department of Biological Sciences, Minnesota State University Mankato, 242 Trafton Science Center South, Mankato, MN 56001, USA
[e]Department of Pharmacology & Therapeutics, McGill University, 3655 Promenade Sir-William-Osler, Montreal, QC H3G 1Y6, Canada
[f]Department of Structural Biology, Molecular Biology Institute of Barcelona, Spanish Research Council, Barcelona Science Park, Barcelona E-08028, Spain
[g]Department of Microbiology, Faculty of Biochemistry, Biophysics and Biotechnology, Jagiellonian University, Gronostajowa 7, Kraków PL-30-387, Poland
[h]Department of Oral Immunology and Infectious Diseases, School of Dentistry, University of Louisville, 501 S Preston St, Louisville, KY 40202, USA
[i]Department of Biological Sciences, Xi'an Jiaotong-Liverpool University, 111 Ren'ai Road, Suzhou Dushu Lake Science and Education Innovation District, Suzhou Industrial Park, Suzhou, Jiangsu 215123, China
*To whom correspondence should be addressed: Email: natalie.zeytuni@mcgill.ca
Edited By David Brenner

Abstract

The type IX secretion system (T9SS) is a nanomachinery utilized by bacterial pathogens to facilitate infection. The system is regulated by a signaling cascade serving as its activation switch. A pivotal member in this cascade, the response regulator protein PorX, represents a promising drug target to prevent the secretion of virulence factors. Here, we provide a comprehensive characterization of PorX both *in vitro* and *in vivo*. First, our structural studies revealed PorX harbors a unique enzymatic effector domain, which, surprisingly, shares structural similarities with the alkaline phosphatase superfamily, involved in nucleotide and lipid signaling pathways. Importantly, such pathways have not been associated with the T9SS until now. Enzymatic characterization of PorX's effector domain revealed a zinc-dependent phosphodiesterase activity, with active site dimensions suitable to accommodate a large substrate. Unlike typical response regulators that dimerize via their receiver domain upon phosphorylation, we found that zinc can also induce conformational changes and promote PorX's dimerization via an unexpected interface. These findings suggest that PorX can serve as a cellular zinc sensor, broadening our understanding of its regulatory mechanisms. Despite the strict conservation of PorX in T9SS-utilizing bacteria, we demonstrate that PorX is essential for virulence factors secretion in *Porphyromonas gingivalis* and affects metabolic enzymes secretion in the nonpathogenic *Flavobacterium johnsoniae*, but not for the secretion of gliding adhesins. Overall, this study advances our structural and functional understanding of PorX, highlighting its potential as a druggable target for intervention strategies aimed at disrupting the T9SS and mitigating virulence in pathogenic species.

Keywords: type IX secretion system, response regulator, alkaline phosphatase, *Porphyromonas gingivalis*, bacterial pathogenicity

---

Significance Statement

Bacterial oral pathogens use a sophisticated protein machinery called the type IX secretion system (T9SS) to deliver virulence factors and promote infection. Our study focuses on the PorX regulatory protein, which acts as the activation switch for the entire secretion system. Through detailed structure and function analyses, our study reveals that PorX has an untypical enzymatic domain similar to known cellular signaling enzymes that were not previously described for the T9SS. We discovered that PorX can also respond to elevated zinc concentrations, reflected by induced dimerization and conformational changes. Our findings provide compelling evidence that PorX is a promising drug target to disrupt virulence factor secretion and reduce bacterial pathogenicity, making this research valuable for advancing treatment strategies against pathogenic bacteria.

Introduction

Porphyromonas gingivalis is the keystone bacterial pathogen in periodontitis, a chronic inflammatory disease of the tooth-supporting tissues (1). Periodontitis affects nearly half of the world's population and ranks as the sixth most prevalent disease globally. Disease manifestation results from bacterial plaque products

directly affecting the periodontium along with the induction of the host's inflammatory and immune responses (2). Chronic exposure to these destructive processes leads to connective tissue destruction, periodontal pocket formation, alveolar bone loss, and even edentulation (3). In addition to *P. gingivalis*'s significant role in periodontitis, other epidemiological and experimental studies have linked its infection and virulence factors secretion to other systemic conditions, including cardiovascular diseases, rheumatoid arthritis, preterm low birth weight, nonalcoholic fatty liver disease, cancer, and Alzheimer's disease (4–9).

P. gingivalis manifests its infection by the secretion of potent virulence factors that promote tissue invasion and destruction, as well as interference with the host's defense systems (10). Among these virulence factors, a group of cysteine proteases, called gingipains, are considered essential to its survival and pathogenicity. These proteases with trypsin-like activity allow this bacterium to escape immune defenses via the cleavage and degradation of host receptors, immunomodulatory proteins, signaling pathway regulatory proteins, and adhesion molecules (11). Gingipain secretion is mediated by a unique type IX secretion system (T9SS) which includes two distinct steps. Initially, the gingipains are translocated across the bacterial inner membrane by the general Sec machinery. Then, once in the periplasm, the gingipains are directed by a conserved C-terminal domain to the specialized T9SS translocon located at the outer membrane. Following the translocation across the outer membrane, the proteins are further processed to remove the conserved C-terminal shuttling domain that is simultaneously replaced with an anionic lipopolysaccharide and remains attached to the bacterial surface or are subsequently released into the extracellular milieu via outer membrane vesicles (12).

Aside from its role in periodontal and systemic disease manifestation in humans, the T9SS is the export apparatus for various virulence factors of different bacterial pathogens, favoring disease dissemination and manifestation in fish and birds (13–16). Notably, the T9SS also presents additional physiological roles in nonpathogenic bacterial species of the Fibrobacteres–Chlorobi–Bacteroidetes superphylum, as highlighted by Mark and Zhu (17). For instance, in the soil bacterium, *Flavobacterium johnsoniae*, the T9SS enables a unique mode of gliding motility through the secretion of specialized adhesins (18) and facilitates the degradation of polysaccharides such as chitin by specialized digestive enzymes secretion (19, 20).

To date, 18 conserved proteins were identified to govern the T9SS function (21). Deletion of any of these genes resulted in the accumulation of cargo proteins in the periplasm, a hallmark of a dysfunctional T9SS. Microbial and biochemical studies have further assigned these essential T9SS members into four functional groups involved in: (i) regulation, (ii) assembly of the core T9SS structures across the inner and outer membranes, (iii) cargo translocation across the outer membrane, and (iv) posttranslational modification of the cargo protein (10). Among the regulatory group of protein components, conserved proteins consisting of a two-component system (TCS) and an additional sigma factor were identified. TCSs are the primary multistep signaling pathways in bacteria, and their minimal composition includes an input sensor histidine kinase (SHK) and an output response regulator (RR). Signal transduction via the TCS relies on phosphoryl-transfer reactions and includes SHK autophosphorylation, phosphoryl group transfer to the RR, followed by RR dephosphorylation (22). The RR component comprises a conserved receiver domain that undergoes phosphorylation and variable output effector domain(s). While most of RR's effector domains function as DNA-binding transcription factors, some exhibit RNA-binding, protein-binding, or even enzymatic activities (23).

Recent studies in *P. gingivalis* suggest that the perception of an unidentified signal in the periplasm leads to the autophosphorylation of the T9SS-SHK, PorY protein (24). The phosphorylated PorY then continues to trans-phosphorylate the T9SS-RR, PorX protein (24). Unlike canonical bacterial TCSs, PorY and PorX are not located within the same operon and are therefore considered orphan SHK and RR, respectively (22, 25–27). Notably, PorX also lacks the classical DNA-binding effector domain and instead possesses an enzymatic effector domain of an unknown function *in vivo*. To promote signal transduction through the pathway and regulate gene transcription, PorX interacts with the SigP transcription factor, which then binds directly to the promoter regions of T9SS genes (27, 28). This regulatory pathway model was further supported by the observation that either *porX* or *sigP* genes deletion resulted in the downregulation of T9SS components and activity, impaired processing of gingipains as well as decreased toxicity (29). Remarkably, this regulatory cascade not only directs the transcription levels of conserved T9SS machinery components but also directly modulates the inner membrane T9SS rotary motor, driving virulence factors secretion across the outer membrane. This reported link between the regulatory pathway and the cargo secretion motor (part of core T9SS structures across the inner and outer membranes) relies solely on interaction between the PorX protein and the cytoplasmic domain of the rotary core component protein, PorL (26). It has been speculated that the PorX–PorL mode of interaction shares similarities with the regulation of the flagella rotary motor by the RR, CheY, in other bacteria (26).

While studies to date have highlighted PorX as the hub protein governing both transcription and motor functions of the entire T9SS, our recent investigation of PorX from *P. gingivalis* (PorX$_{PG}$) unveiled its ability to hydrolyze crucial signaling molecules like cyclic and linear oligoadenylates (30). Despite these advancements, the precise role and mechanism by which this atypical RR mediates signal transduction through the cascade remains unknown. Here, we report the structure determination and functional analysis of the PorX protein from the gliding bacterium *F. johnsoniae* (PorX$_{FJ}$) as a model system. Our crystal structures reveal that the PorX$_{FJ}$ adopts a two-domain dimeric fold with a classical RR receiver domain's fold and a unique alkaline phosphatase superfamily (APS) domain connected by a helical linker region. Our functional characterization *in vitro* shows that PorX$_{FJ}$ can be activated by dimerizing either upon phosphorylation at the receiver domain or by zinc binding at the APS domain, suggesting a plausible dual activation cellular signal. Next, we demonstrate a functional complementation between the PorX$_{FJ}$ from the nonpathogenic *F. johnsoniae* bacterium to PorX$_{PG}$ from the pathogenic *P. gingivalis*. Accordingly, we further translate the obtained structural and functional knowledge to investigate PorX's role in *P. gingivalis*. Accordingly, we find that conformational alterations in the APS domain induced by zinc, rather than its phosphodiesterase catalytic function, have a more pronounced impact on T9SS functionality in *P. gingivalis*. Together, our results mark a significant milestone in the characterization and understanding of the role of this critical hub protein in virulence factors secretion.

Star methods

Recombinant protein expression and purification in *Escherichia coli*

Construction of expression plasmids

The full-length Fjoh_2906 (UniProt A5FFU4) gene was amplified by PCR from *F. johnsoniae* ATCC 17061 strain UW101 genomic DNA. The restriction-free method (31) was used to insert the amplified

gene into a modified pET28a(+) vector (Novagen). In the expression vector, the gene was fused in frame to an N-terminal 10×-His-tag followed by a thrombin proteolytic site. Site-directed mutagenesis was performed by Gibson assembly (32). All primers and plasmids used in this study are listed in Tables S1 and S2, respectively.

Bacterial cultivation and protein expression

E. coli BL21 strain cells harboring pET28a(+)-PorX$_{FJ}$ variants (wild type and mutants) were cultivated in an autoinduction medium (33) containing kanamycin (50 µg/mL) at 37°C for 8 h. The cultivation temperature was lowered to 22°C and expression continued for another 16 h. The cells were harvested by centrifugation at 6,000×g for 15 min at 4°C.

Recombinant protein purification

PorX$_{FJ}$ variants were purified as previously described (34). Briefly, cell pellets were resuspended in buffer A (50 mM Tris pH 8, 300 mM NaCl, and 10 mM imidazole) and incubated with DNase I (10 mg/mL) and protease inhibitor cocktail (Calbiochem) at 4°C. The cells were then disrupted by two cycles in a French press pressure cell at 172 MPa. Cell debris was removed by high-speed centrifugation at 270,000×g for 1 h at 4°C. The supernatant was applied to a gravity nickel-nitrilotriacetic (Ni-NTA) column (Bio-Rad Econo-Column chromatography column, Thermo Scientific HisPur Ni-NTA resin) pre-equilibrated with buffer A. The bound protein was washed with buffers B (20 mM Tris pH 8, 300 mM NaCl, and 20 mM imidazole) and C (20 mM Tris pH 8, 1 M NaCl, and 40 mM imidazole) and eluted with buffer D (20 mM Tris pH 8, 200 mM NaCl, and 500 mM imidazole). To cleave the His-tag, bovine thrombin (Prolytix) was added to the eluted protein and the mixture was then dialyzed against buffer E (20 mM Tris pH 8 and 200 mM NaCl) for 16 h at 4°C. The protein was then applied onto a size exclusion column (Superdex 200 16/60 GL, Cytivia) pre-equilibrated with buffer E. The purified proteins were concentrated to ∼25 mg/mL and flash-frozen in liquid nitrogen.

Crystallization and structure determination

Wild-type PorX$_{FJ}$ and the T271V mutant were each crystallized using the sitting drop vapor diffusion method at 25°C. In brief, 0.2 µL of 5 mg/mL protein solution was mixed with an equal volume of precipitant solution. Native PorX$_{FJ}$ was crystallized in two different conditions. Detailed crystallization conditions and individual data collection parameters for each crystal are listed in Table S3. For phasing, the PorX$_{FJ}$ primitive orthorhombic crystal form was soaked for 15 s in a precipitant solution containing 0.5 M sodium bromide, and multiwavelength anomalous diffraction datasets were collected. All datasets were reduced and scaled using the HKL2000 suite (35), and phases were obtained using CRANK2 (36). The initial model was manually built in Coot (37) according to the electron density map calculated from data collected at the peak wavelength of bromide. This initial atomic model was used as a template for molecular replacement in Phaser (38) against all other datasets. The final models were manually edited in Coot (37) and refined by Refmac5 (39). For R_{free} calculations, 5% of the data were excluded. All structural figures were prepared using Chimera (40). Data collection and refinement parameters are listed in Table S4.

Protein phosphorylation assay *in vitro*

For intact protein mass spectrometry, purified PorX$_{FJ}$ variants were incubated at 100 µM in buffer F (25 mM Tris pH 7.5, 10 mM MgCl$_2$, 1 mM MnCl$_2$, 2 mM dithiothreitol [DTT], 5 mM acetyl phosphate [AcP], and 0.01 mM sodium orthovanadate). After 20 min at 37°C (or 1 h at room temperature for PorX$_{FJ}$ D54A/T271V due to precipitation issues), the reactions were quenched by flash-freezing in liquid nitrogen.

Intact protein liquid chromatography–mass spectrometry

As previously described (41–43), protein samples were diluted to 0.1 mg/mL in 0.1% (v/v) formic acid before 1 µg was injected on a Dionex Ultimate 3000 UHPLC system at 40 µL/min using a Waters Acquity BEH C4 BEH column (300Å, 1.7 µM, 1× 100 mm). The resulting eluate (5-min wash with 4% [v/v] acetonitrile followed by 15-min gradient of 4–90% [v/v] acetonitrile in 0.1% [v/v] formic acid) was analyzed on an Impact II QTOF mass spectrometer (Bruker Daltonics) equipped with an Apollo II ion funnel electrospray ionization source and Bruker otofControl v4.0/DataAnalysis v4.3 software. Data were acquired in positive-ion profile mode using a capillary voltage of 4,500 V and dry nitrogen heated at 200°C. Total ion chromatograms were used to determine where the protein eluted and spectra were summed over the entire elution peak. Multiple charged ion species were deconvoluted at 5,000 resolution using the maximum entropy method.

Functional characterization in *P. gingivalis*

Bacterial strains, plasmids, and growth conditions

The wild-type strain used in this study was *P. gingivalis* W50. The wild-type bacterium and mutants were propagated from −80°C freezer stocks and grown anaerobically at 37°C for 3–5 days on agar plates containing trypticase soy broth (TSB) (Becton, Dickinson and Company, Franklin Lakes, NJ, USA) supplemented with 5 µg/mL hemin, 1 µg/mL menadione, and 5% defibrinated sheep blood (BAPHK) (Northeast Laboratory Services, Winslow, ME, USA). The atmosphere of the anaerobic chamber contained a mixture of 5% hydrogen, 10% carbon dioxide, and 85% nitrogen. The bacterial colonies were used for making starter cultures in TSB liquid media supplemented with 5 µg/mL hemin and 1 µg/mL menadione that were then grown anaerobically at 37°C without shaking.

Construction of the deletion mutants in P. gingivalis

Mutant strain W50 $\Delta porX_{PG}$ was generated as previously described (44). In order to construct the $\Delta porX_{PG}$ mutant, 1-kb-long regions both upstream and downstream of $porX_{PG}$ were amplified from W50 genomic DNA and the erythromycin resistance gene (*emrF*) was amplified from plasmid pVA2198 by PCR. The three amplicons were purified and combined using the NEBuilder HiFi DNA Assembly Master Mix (New England BioLabs, Ipswich, MA, USA) according to the instructions provided by the manufacturer. The final product was transformed into *P. gingivalis* by electroporation. The transformed cells containing the erythromycin resistance gene in the site of $porX_{PG}$ were selected by growth on BAPHK medium containing 10 µg/mL erythromycin.

To complement the $porX_{PG}$ deletion mutant, $porX_{PG}$ and $porX_{FJ}$ were cloned separately into plasmid pT-COW and placed under the control of a low-level constitutive promoter (groES [PG0521] promoter region), generating pT-groES-$porX_{PG}$ and pT-groES-$porX_{FJ}$, respectively. To generate all truncations and point mutations of $PorX_{PG}$, the pT-groES-$porX_{PG}$ plasmid was used. The pT-groES-$porX_{PG}$ constructions with different mutations on the $porX_{PG}$ region were then transformed into *E. coli* S17-1 cells for the conjugation with $\Delta porX_{PG}$ mutant. All complemented strains were generated by conjugation as previously described (45). In brief, BAPHK containing

tetracycline (1 μg/mL) was used to select for pT-groES-*porX*$_{PG}$ containing *P. gingivalis* strains, and gentamicin (200 μg/mL) was used to counter-select the *E. coli* S17-1 donor. Transconjugants were obtained after 7 days of anaerobic incubation, and the transconjugants were isolated, verified by PCR, and maintained on BAPHK containing tetracycline (1 μg/mL). All primers and plasmids used in this study are listed in Tables S1 and S2, respectively.

Gingipain enzymatic activity assay

Wild-type *P. gingivalis* W50, PorX null mutant cells carrying empty pT-COW plasmids, and all pT-groES-*porX*$_{PG}$ constructs carrying the different mutations of *porX*$_{PG}$ were cultivated to OD$_{600}$ of 1.0. The cultures were harvested and screened for their gingipain activities. Arginine–gingipain (Rgp) and lysine–gingipain (Kgp) assays were carried out according to previously described methods (46) with slight modifications. For the Rgp assay, 10 μL of liquid culture was mixed with 170 μL of buffer H (200 mM Tris HCl, pH 7.6, 150 mM NaCl, 5 mM CaCl$_2$, 0.02% NaN$_3$, and 20 mM L-cysteine previously neutralized with 8 M NaOH in a 9:1 ratio). In the case of the Kgp assay, 50 μL liquid culture was mixed with 130 μL buffer H. The mixtures were incubated at 37°C for 10 min followed by the addition of 1 mM substrate (Nα-benzoyl-L-arginine 4-nitroanilide hydrochloride for the Rgp assay and 2-acetamido-6-amino-*N*-(4-nitrophenyl) hexanamide for the Kgp assay). The formation of p-nitroaniline product was measured at 405 nm at 1-min intervals for 30 min with constant shaking. All assays were performed in quadruplicates.

Expression levels validation by western blot

Wild-type *P. gingivalis* W50 and plasmid complemented null *porX* strains were cultivated to OD$_{600}$ of 1.0. The cultures were harvested and resuspended in phosphate-buffered saline (PBS) supplemented with 2 mM of Nα-tosyl-L-lysine chloromethyl ketone hydrochloride (Sigma) and protease inhibitor cocktail (Calbiochem) to inactivate all gingipains prior to lysis. The resuspended cells were sonicated and boiled in SDS–PAGE sample buffer without DTT for 3 min. The samples were boiled again for additional 3 min following the addition of DTT to a final concentration of 20 mM. Samples were centrifuged briefly at 13,000 × *g* for 1 min to remove particulates and the supernatants were separated on SDS–PAGE. Proteins were subsequently electro-transferred onto a Polyvinylidene fluoride (PVDF) membrane pre treated with methanol and blocked overnight in a solution containing Tris-buffered saline with 0.1% Tween 20 (TBST) and 5% (w/v) skimmed milk. Rabbit polyclonal anti-PorX$_{PG}$ antibodies were manufactured by ProteoGenix (Schiltigheim, France) using recombinant PorX as an antigen. PorX$_{PG}$ was detected using the anti-PorX$_{PG}$ (1 μg/mL) in TBST supplemented with 5% skimmed milk for 90 min. Membranes were washed three times with TBST before being probed for 60 min with a 1:10,000 dilution of a polyclonal goat antirabbit horseradish peroxidase-conjugated secondary antibody (Invitrogen) in 5% skimmed milk/TBST. Development was carried out using the enhanced chemiluminescence (ECL) western blot substrate kit according to the manufacturer's instructions (Millipore). The biotinylated inner membrane-associated protein MmdC was used as a loading control (47). The membrane was blocked in a TBST solution containing 2% Bovine serum albumin (BSA) and detected by a 1:4,000 dilution of streptavidin conjugated to horseradish peroxidase (Thermo Scientific).

Functional characterization in *F. johnsoniae* and other *in vitro* assays

See details in the Supplementary Materials.

Results

PorX is a conserved protein found in some pathogenic and nonpathogenic bacterial species commonly known to utilize their T9SS for protein cargo secretion. In an effort to determine the structure of PorX, we have applied an orthologue screening approach (34). Orthologue screening is a well-established strategy to improve the expression, purification, and structural determination of challenging proteins (48). Among the different orthologues screened (34), we identified two distinctive conditions promoting the crystallization of the full-length PorX from *F. johnsoniae* (PorX$_{FJ}$) in its nonphosphorylated apo-form. Heavy-atom derivative (bromide) soaking, followed by a multiwavelength anomalous diffraction data collection, were used to retrieve the missing phase information and solve the high-resolution structure of PorX$_{FJ}$ (Tables S3 and S4).

Overall structure

Although the purified nonphosphorylated PorX$_{FJ}$ was found to be monomeric in solution by size exclusion chromatography (34), both crystal forms presented an identical dimeric assembly within their asymmetric units (Fig. 1). The primitive orthorhombic crystal form gave rise to a single dimeric assembly (two monomers in the asymmetric unit), while the primitive monoclinic crystal form gave rise to two identical dimeric assemblies (four monomers in the asymmetric unit) (Fig. S1A–C). All PorX$_{FJ}$ dimers adopt an intertwined assembly, where each monomer is symmetrically wrapped around the other monomer, forming an overall "X"-like shape (Fig. 1A). The formation of these identical assemblies (Cα's RMSD = 0.98–2.35 Å^2) suggests that the observed dimer represents a true functional state that was unlikely driven by crystal packing.

Monomeric structure

Each PorX$_{FJ}$ monomer adopts a two-lobed fold containing an N-terminal receiver (REC) domain (residues 1–120), followed by a three-helix bundle (THB) domain (residues 121–209) and a C-terminal APS domain (residues 210–517) (Fig. 1A). All of the determined PorX$_{FJ}$ monomers exhibit a high degree of structural similarity with a Cα RMSD ranging from 0.64 to 2.05 Å^2. The minute structural variations observed primarily stem from the flexibility in the positioning of the REC domain relative to the THB and APS domains (Fig. S1D and E).

The highly conserved fold of the REC domain includes five α-helices (α1–α5) that surround five central parallel β-strands (β1–β5). Within the REC domain, the surface exposed phosphorylation site involves residues Asp10, Asp11, Asp54, Thr82, and Lys104 that together coordinate the binding of a divalent cation and the phosphate moiety (Fig. 1B).

The THB domain interconnects the REC domain and the APS domain as it gives rise to the formation of the "X"-shaped dimer (Fig. 1A). In particular, the entire THB domain curves ∼75° away from the REC domain via its α1 helix that packs against the REC domain of the adjacent monomer, while utilizing its α2 and α3 to pack against and support the subsequent APS domain.

At the C terminal of PorX$_{FJ}$, the APS domain comprises a β-sheet flanked by α-helices (canonical $(\alpha/\beta)_6$ APS fold) and an additional β-strand rich capping region, also known as the cap subdomain (Fig. 1A). The APS catalytic site is characterized by two divalent cations essential for catalysis and located within a shallow groove, where the substrate is predicted to bind. The two cations are coordinated by seven highly conserved residues: Asp360, His364, and His499 coordinates cation binding at the first site (Zn1), while
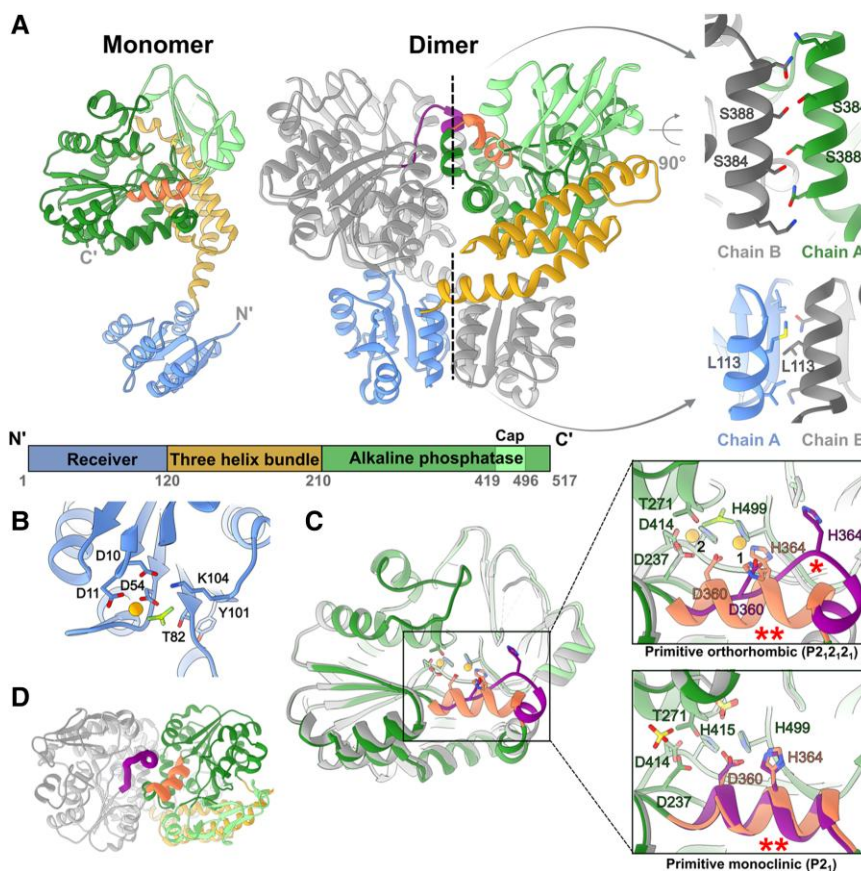
Fig. 1. Crystal structures of PorX$_{FJ}$. A) Monomeric and dimeric assembly of PorX$_{FJ}$. One monomer is colored according to the different domains, while the other monomer is in gray. The two dimeric interfaces are labeled by dashed lines, and their zoom-in views highlight crucial residues at these dimerization interfaces. B) Phosphorylation site at the REC domain. The conserved Asp54 coordinates both the phosphomimetic BeF$_3$ molecule and a divalent cation presented as an orange sphere. Additional residues involved in coordination and stabilization of the phosphorylation site are presented. C) Structural variation of the APS domain in the different monomers. Overlay of different APS domain conformers demonstrate the observed conformational change in residues 358–369. In the zoom-in views of the catalytic site, key residues associated with the coordination of two divalent cations (binding sites labeled as 1 and 2) and substrate binding/catalysis are presented. The substrate-mimicking BeF$_3$ ion (shades of green) or sulfate ion (yellow), specifically identified in different PorX$_{FJ}$ crystals, is presented separately. The alternative conformation of residues 358–369, labeled by (*), disrupts the optimal positioning of the conserved divalent cation coordinating residues, Asp360 and His364. The helical conformation of residues 358–369, which maintains the ideal position of Asp360 and His364, is labeled by (**). D) A top view of the APS domains in the PorX$_{FJ}$ dimer demonstrates a conformational change in residues 358–369 (colored in purple and orange in each monomer), located in close proximity to the APS domain dimerization interface.

Asp237, Asp414, and His415 and the catalytic nucleophile Thr271 coordinates cation binding at the second site (Zn2, sites nomenclature according to (49)) (Fig. 1D). Within the dimer, both APS catalytic sites are facing each other and are in close proximity to the dimeric interface (Fig. 1A). The divalent cation's identity was confirmed by a co-crystallization in the presence of zinc and anomalous diffraction analysis (Tables S3 and S4). In addition, zinc binding was confirmed by inductively coupled plasma mass spectrometry (ICP-MS) revealing 2.02 zinc ions bound per each monomer. Zinc binding affinity was further analyzed by isothermal titration calorimetry (ITC) and conformed to a two-site binding model with the following stoichiometries (N) and equilibrium dissociation constants (K_D): $N_1 = 1.09 \pm 0.04$ and $K_{D1} = 180.83 \pm 14.93$ nM; $N_2 = 1.19 \pm 0.04$ and $K_{D2} = 59.17 \pm 13.81$ nM (Fig. S2).

Dimeric interfaces

Two major interfaces mediate the formation of the intertwined dimer; the first is formed by the two identical REC domains (952 Å^2), while the other is formed by the two APS domains (∼ 1,000 Å^2) (Fig. 1A). Notably, the phosphorylation and activation of canonical RRs lead to their dimerization via local conformational changes in two conserved REC domain residues. The induced dimerization then renders the downstream activities of the RR (23). Multiple RR crystal structures have unambiguously demonstrated that conserved threonine (T) and tyrosine (Y) residues, also known as the TY pair of the REC domain, undergo conformational changes upon the domain's phosphorylation and are indicative of its activation state (23). In the nonphosphorylated state, the side chain of the conserved threonine faces the solvent, while in the phosphorylated state, it is reoriented toward the phosphorylation site, thus creating a space to accommodate the conserved tyrosine side chain. These local conformational changes give rise to the formation of the REC domain dimers. Here, the positioning of the REC domain's TY pair (Thr82 and Tyr101) clearly indicates that the formed dimer represents the activated state (Fig. S3A).

To further assess whether the observed dimer truly represents the phosphorylated/activated state, we have co-crystallized PorX$_{FJ}$ with the phosphate analog, BeF$_3$ (Tables S3 and S4). In the presence of BeF$_3$, PorX$_{FJ}$ continued to adopt the same "X"-shaped dimer with a clear density that can be attributed to the analog observed at the REC domain's phosphorylation site (Figs. 1B and S3B). In addition, in the primitive monoclinic crystal form, spherical densities, in dimensions suitable to accommodate sulfate ion (mimicking phosphate ion)

originating from the crystallization condition, were clearly observed in the REC domain phosphorylation site (Fig. S3B). These observed phosphate-analog densities at the REC phosphorylation site were also found in similar positions to the phosphate moiety observed in the determined structure of the phosphorylated Spo0A RR (50). Taken together, we conclude that the observed dimeric fold truly represents the functionally activated state.

The two APS domains give rise to the second dimerization interface of the intertwined dimer (Fig. 1A). The APS dimeric interface comprises symmetrical interaction between helix α17 (residues 378–393) and residues 358–369 (Figs. 1A and S4). Despite the overall conserved fold of the APS domain (RMSD = 0.88 Å^2), one area of significant difference specifically involves residues 358–369 (Fig. 1C and D). In the primitive orthorhombic crystal form, residues 358–369 adopt a helical conformation in one monomer while presenting an extended coil conformation and an additional helical turn at the N terminal of helix α16 in the second monomer (Fig. 1C and D). Moreover, in one of the monomers of the primitive monoclinic crystal form, residues 358–369 were flexible and their backbone could not be traced in the density map, while in the other monomers they adopted a helical conformation, further establishing the dynamic nature of this area of the protein (Fig. 1D). Global comparison of the APS dimerization interface demonstrates that the 358–369 helical-extended coil conformation dyad gives rise to a total of 1,080 Å^2 surface area, while the helical–helical conformations dyad interface is only 993 Å^2, suggesting the helical-extended loop conformation to be more stable.

Within each dimer, both APS active sites are located in close proximity to the dimeric interaction interface (Fig. 1A and C). Therefore, changes in the conformational state of the 358–369 region can significantly impact the zinc ion coordination of catalytic site (Fig. 1D). In particular, only the helical conformation of residues 358–369 can support the proper coordination of the Zn1 by the conserved Asp360 and His364 residues, whereas in the extended coil conformation, these residues are facing away from the APS catalytic site (Fig. 1D). Additional support to the link between metal coordination

and residues 358–369 conformation is provided by the T271V APS catalytically inactive mutant structure (Tables S3 and S4). In the T271V structure, a density corresponding to a divalent cation could only be observed in Zn1 site (coordinated by Asp360, His364, and His499) and not in the Zn2 site (coordinated by Thr271, Asp237, Asp414, and His415) (Fig. S5A), while residues 358–369 of both monomers adopted a helical conformation instead of the helical-extended coil dyad observed in the same primitive orthorhombic crystal form of the wild type. Moreover, ICP-MS measurements revealed that the T271V mutant had a reduced ability to bind zinc with only 1.22 ions per monomer, instead of two seen by the wild type. The ICP-MS measurements of the D360A/H364A double mutant further demonstrated a reduction in zinc binding capacity (0.63 zinc ions per monomer), suggesting that the zinc binding at the Zn1 site stabilizes the binding in the Zn2 site. Interestingly, abolishing the APS dimeric interface by the S348A/S388E double mutant also reduced the zinc binding capacity to 1.03 zinc ions per monomer, thus further establishing the link between zinc binding at the APS domain and its dimer interface. Based on the observed conformational dynamics and the association with zinc binding, we speculate that this region might provide an additional level of regulation to the catalytic activity of the APS domain.

Insights for substrate binding and catalytic activity of the APS domain

Structural comparison of the APS domain revealed a remarkable fold similarity to the APS that can hydrolyze P–O, S–O, or P–C bonds while possessing a bi-metal zinc coordination architecture at their active site. Among these identified homologs, PhnA is a bacterial enzyme involved in a metabolic pathway that converts phosphonates to phosphorus and directly catalyzes phosphonoacetate to acetate and inorganic phosphate (51) (Fig. 2A). The other homologs belong to the ectonucleotide pyrophosphatase/phosphodiesterase (ENPP) family (49, 52–57) (Fig. 2A). The ENPP family members (ENPP1-7) can be found in both bacteria and eukaryotes, where they participate in different cellular processes,
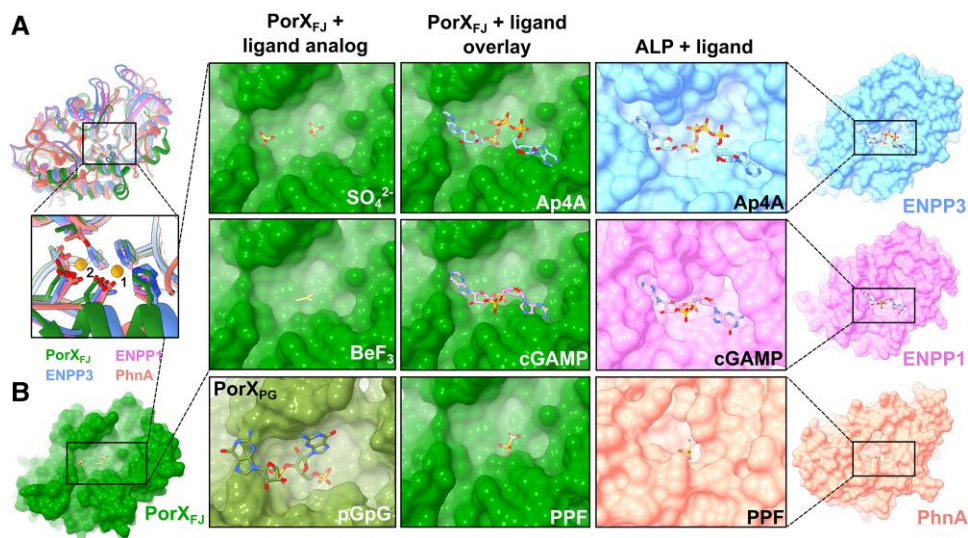

Fig. 2. Structural similarities of PorX$_{FJ}$'s APS domain points toward its substrate specificity. A) Overlay of the APS domains of PorX$_{FJ}$, ENPP3, ENPP1, and PhnA demonstrates their conserved overall fold. Zoom-in view of their catalytic sites including the conserved bi-metal coordination, substrate binding, and catalysis residues. B) Surface representation of APS domains catalytic pockets exhibiting a clear correlation between the ligand and binding pocket dimensions. The APS domain of PorX$_{FJ}$ with its determined ligand analogs (SO$_4^{2-}$ and BeF$_3$) in green. PorX$_{PG}$ with 5'-phosphoguanylyl-(3'→5')-guanosine (pGpG) bound in olive green (PDB ID: 7PVK). The ENPP3 with bis(adenosine)-5'-tetraphosphate (Ap4A) polynucleotide bound (PDB ID: 6F2Y) in blue, the ENPP1 with adenosine–guanosine-3',3'-cyclic monophosphate (cGAMP) bound (PDB ID: 6AEL) in pink, while PhNA with phosphonoformate bound (PDB ID: 1EI6) is in orange. Overlay of PorX$_{FJ}$ with the ligand-bound ENPPs or PhnA suggests that the APS domain of PorX$_{FJ}$ can accommodate a large polyphosphate substrate.

including nucleotide hydrolysis, lipid metabolism, and associated signaling transduction pathways (58). Apart from the highly conserved residues associated with the catalytic mechanism and the two zinc ions coordination (Thr271, Asp360, His364, His499, Asp237, Asp414, and His415), the potential substrate binding pockets displayed some degree of variation depending on their specific substrate. In particular, ENPPs that are involved in oligonucleotide hydrolysis displayed the most extensive cavities, while PhnA displayed the smallest cavity, compatible with the small size of the phosphonoacetate substrate (Fig. 2B). Here, our structural comparisons revealed that the APS site binding pocket of PorX$_{FJ}$ is extensive and is, therefore, likely to bind a large substrate (Fig. 2B). In support of this notion, in the primitive monoclinic crystal form, two phospho-mimicking sulfate ions were identified and modeled at PorX$_{FJ}$'s APS binding cavity (Figs. 2B and S5B). One sulfate ion was modeled next to the catalytic Thr271, while the other was located in an auxiliary binding cleft and stabilized by Arg275, Lys329, and Asn357. These findings further suggest that PorX$_{FJ}$'s potential ligand might not only be large but also include polyphosphate moieties such as cyclic di-nucleotides or polynucleotides. Notably, in the primitive orthorhombic crystal form that was co-crystallized with the phosphomimetic ion (Tables S3 and S4), the corresponding density of a single BeF$_3$ molecule was clearly observed in the catalytic site (in close proximity to the catalytic T271) but not in the auxiliary binding site (Figs. 2B and S5C). Notably, the spatial positions of the phosphate analogs identified in our PorX$_{FJ}$ structures align closely with those observed in the recently determined crystallographic structure of catalytically inactive T272V variant of PorX$_{PG}$ bound to phosphoguanylyl-(3′→5′)-guanosine (pGpG) (Figs. 2B and S6). However, our attempts to co-crystalize the catalytically inactive T271V variant of PorX$_{FJ}$ with pGpG did not reveal the corresponding density in the APS catalytic site (Fig. S5A).

Albeit our unsuccessful attempts to capture the structure of PorX$_{FJ}$ in complex with cyclic or polynucleotides, we have confirmed its enzymatic activity by a phosphodiesterase assay. In the assay, full-length PorX$_{FJ}$ and the THB + APS truncation mutant (where the REC domain was truncated) were able to hydrolyze the phosphodiesterase substrate analog bis(p-nitrophenyl) phosphate (bis-pNPP) only in the presence of zinc and not by other divalent cations (Fig. 3A). The phosphodiesterase activity was pH dependent with an optimal pH in the range of 8–9, similar to the APS superfamily (Fig. 3B). Notably, a significant reduction in hydrolysis rate was observed for (p-nitrophenyl) phosphate, while no hydrolysis was observed for the (p-nitrophenyl) sulfate, providing hints toward substrate specificity (Fig. S7). Mutating the catalytic residues T271V, the metal-coordinating residues D360A/H364A,

and the APS dimerization interface residues S384A/S388E, abolished the observed phosphodiesterase activity against bis-pNPP (Fig. 3C). The phosphodiesterase assay further established the importance of zinc coordination and dimerization of the APS domain for catalytic activity.

In vitro phosphorylation and subsequent dimerization of PorX$_{FJ}$ variants

In TCS, canonical response regulators can be phosphorylated *in vitro* by incubation with the potent phosphodonor acetyl phosphate (AcP). Phosphorylation of the conserved Asp residue at the RR's REC domain often leads to its dimerization and further induces its downstream function. Here, incubation with AcP in the presence of Mg^{2+} also led to PorX$_{FJ}$ phosphorylation, as confirmed by intact protein mass spectrometry (liquid chromatography–mass spectrometry [LC–MS]) experiments (Fig. 4, Table S5). Surprisingly, these LC–MS experiments revealed that apart from the predicted Asp54 phosphorylation site, AcP can also phosphorylate Thr271 in PorX$_{FJ}$ (Fig. 4, Table S5). Using the REC domain's phosphorylation-null mutant (D54A), the APS domain's catalytically inactive mutant (T271V) and their double mutant (D54A/T271V), we confirmed that these residues can specifically undergo phosphorylation in PorX$_{FJ}$ (Figs. 4 and S8, Table S5). Interestingly, incubation of the wild-type PorX$_{FJ}$ and certain mutants with AcP (apart from the D54A-phosphorylation-null mutant) led to an 18-Da mass decrease in both the nonphosphorylated and phosphorylated populations (Fig. 4, Table S5). We hypothesized that the observed mass reduction resulted from a dehydration reaction linked to the formation of an internal peptide bond due to nonproductive AcP phosphorylation (Fig. S9). Since the proposed cyclization reaction likely involved an amine group replacing one of the oxygens of Asp54, our molecular modeling identified a lysine residue (Lys104) in close proximity to Asp54 (Fig. 1B). Subsequent, intact LC–MS for the purified K104A mutant eliminated the dehydration reaction (Fig. 4, Table S5), thus validating our proposed alternative cyclization as an alternative AcP mechanism *in vitro*.

Incubation with AcP in the presence of Mg^{2+} also led to PorX$_{FJ}$ dimerization, as revealed by size exclusion chromatography (Fig. 5). Notably, incubation with Mg^{2+} alone did not result in protein dimerization. Mutation of the phosphorylation site in the REC domain (i.e. D54A) also eliminated the AcP-induced dimerization (Fig. 5). Interestingly, the L113E mutation, located at the REC domain dimerization interface, failed to dimerize in the presence of AcP, thus revealing the crucial cross talk between phosphorylation and dimerization of the REC domain (Fig. 5).
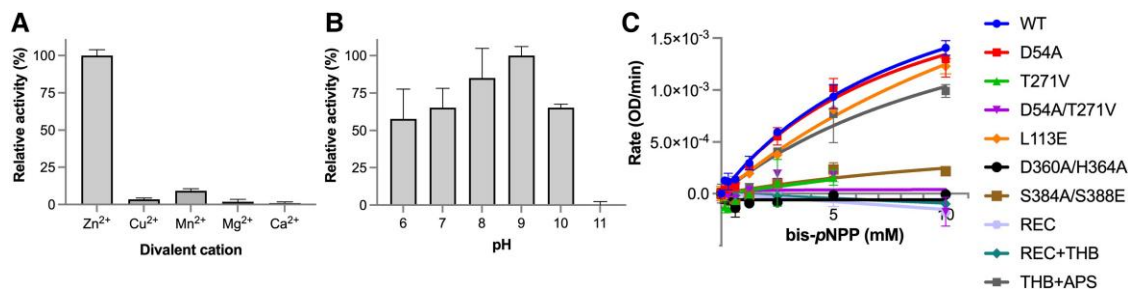

Fig. 3. Phosphodiesterase activity of PorX$_{FJ}$. A Divalent cation and B) pH screening for the identification of optimum conditions of phosphodiesterase activity using bis-pNPP as a substrate. All percentage values in the pH and metal screens are normalized to pH 9 and Zn, respectively. C) Phosphodiesterase kinetics of wild-type PorX$_{FJ}$ and its mutants at increasing concentrations of bis-pNPP.
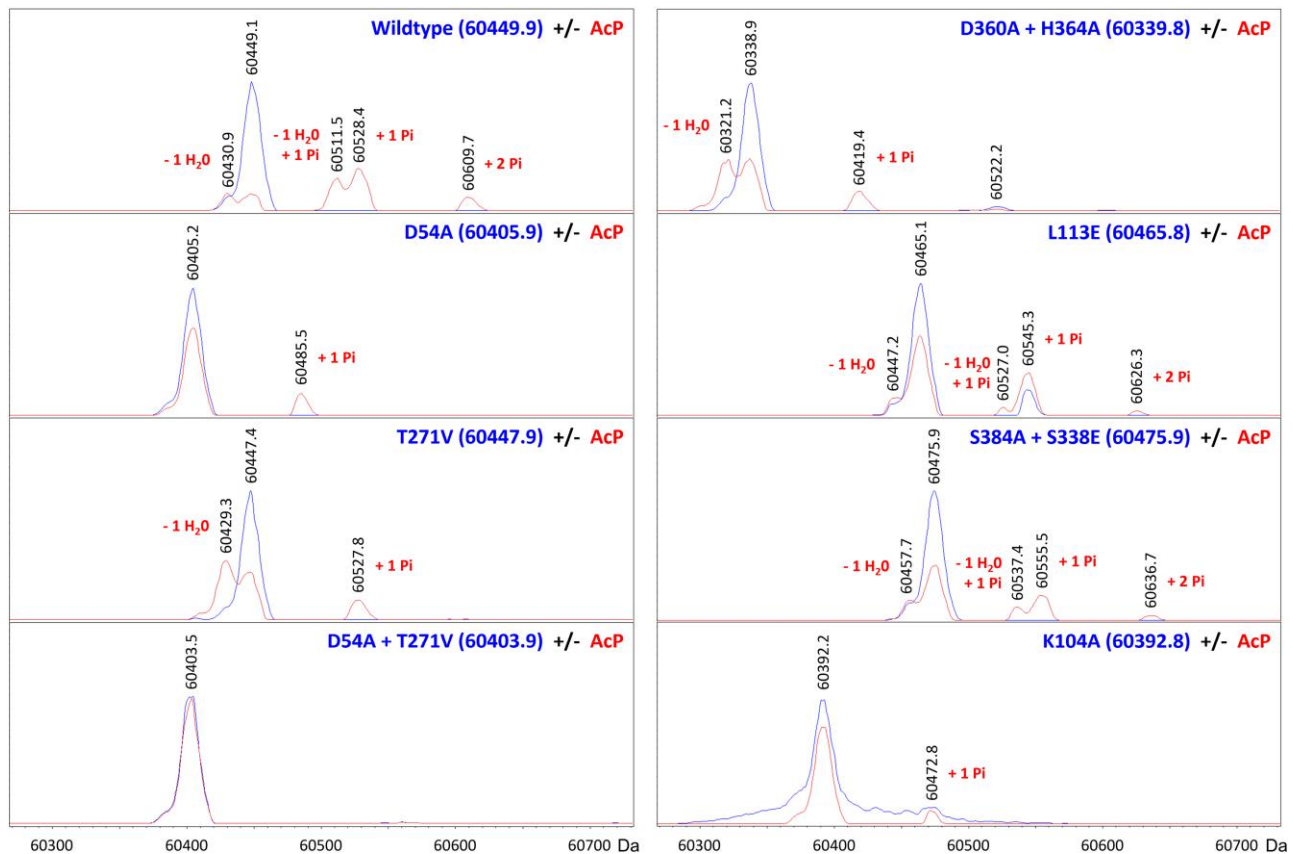
Fig. 4. Intact protein LC–MS analyses of PorX$_{FJ}$ point mutants in the absence or presence of phosphorylation *in vitro*. The blue and red spectra correspond to nonphosphorylated and phosphorylated versions of the protein, respectively. Comparing the theoretical and observed masses (inset blue and black numbers, respectively, in dalton) showed that the acetyl phosphate (AcP) phosphodonor promotes the phosphorylation of Asp54 and/or Thr271 ("+1 Pi" or "+2 Pi" labels). Alternatively, AcP was found to induce cyclization of Asp54 and Lys104, resulting in a dehydration reaction ("− 1 H$_2$0" labels) and subsequent phosphorylation at Thr271 only ("− 1 H$_2$0, + 1 Pi" labels).

Zinc-induced dimerization

In addition to zinc's essential role for the catalytic activity of the APS domain, incubation of PorX$_{FJ}$ with zinc resulted in a clear shift of its monomeric population to dimeric, even in the absence of AcP (Fig. 5). Notably, zinc-induced dimerization is independent of the REC domain's ability to phosphorylate, as the D54A null phosphorylation, the L113E dimerization interface, and the REC domain only truncation variants were still able to dimerize in the presence of zinc (Fig. 5). In contrast, mutations in the APS domain's catalytic site and dimerization interface led to significant alterations in the zinc-induced dimerization ability (Fig. 5), which stands in good agreement with their reduced ability to bind zinc as demonstrated by the ICP-MS measurements. For example, the catalytically inactive T271V variant exhibited a mixed population of both monomers and dimers, while the zinc coordination D360A/H364A double mutant remained mostly monomeric upon incubation with zinc (Fig. 5). Abolishing the APS dimerization interface in the S384A/S388E double mutant also resulted in a significant shift toward the monomeric population (Fig. 5). Interestingly, both the D54A and the T271V individual phosphorylation-null and catalytically inactive variants sustained a restricted ability to dimerize in the presence of zinc (Fig. 5). However, the double catalytic mutant D54A/T271V was not able to dimerize properly (Fig. 5), therefore suggesting a cumulative effect of these mutations in comparison with their single catalytic mutants.

Functional complementation and analysis of PorX in the pathogenic *P. gingivalis*

Deletion of the *porX* gene in *P. gingivalis* leads to a dysfunctional T9SS and subsequently severely impacts gingipains secretion (24, 28). Therefore, monitoring the gingipains secretion by measuring their amidolytic activity serves as a sensitive probe for the T9SS function in *P. gingivalis* (10, 59, 60). Since the orthologous proteins PorX$_{FJ}$ and PorX$_{PG}$ share 51% sequence identity and 71% sequence similarity, we hypothesized that PorX$_{FJ}$ could functionally complement the Δ*porX* deletion strain of *P. gingivalis* (Fig. S4). Using the gingipains amidolytic activity assay (46), we demonstrated that the plasmid complementation of PorX$_{FJ}$ can functionally substitute PorX$_{PG}$, in the background of the Δ*porX*$_{PG}$ deletion strain (Fig. 6A). The observed functional complementation of PorX$_{FJ}$ in *P. gingivalis* provided crucial evidence to our scientific approach as it validates the use of insights obtained from the PorX$_{FJ}$ and the recently determined PorX$_{PG}$ structures (30) to characterize the function of PorX$_{PG}$ in the pathogenic *P. gingivalis*. As such, domains and key residues revealed by our reported PorX$_{FJ}$ high-resolution structure determination are likely to share a similar function and be translatable for PorX$_{PG}$, where their effect on virulence factors secretion can be further assessed *in vivo*.

First, we investigated the role of the PorX's receiver and effector domains on virulence factors secretion in *P. gingivalis*. Here, our gingipains amidolytic activity assay revealed that the deletion of either the APS domain (PorX$_{PG}$ Δresidues 208–517), the THB and the APS
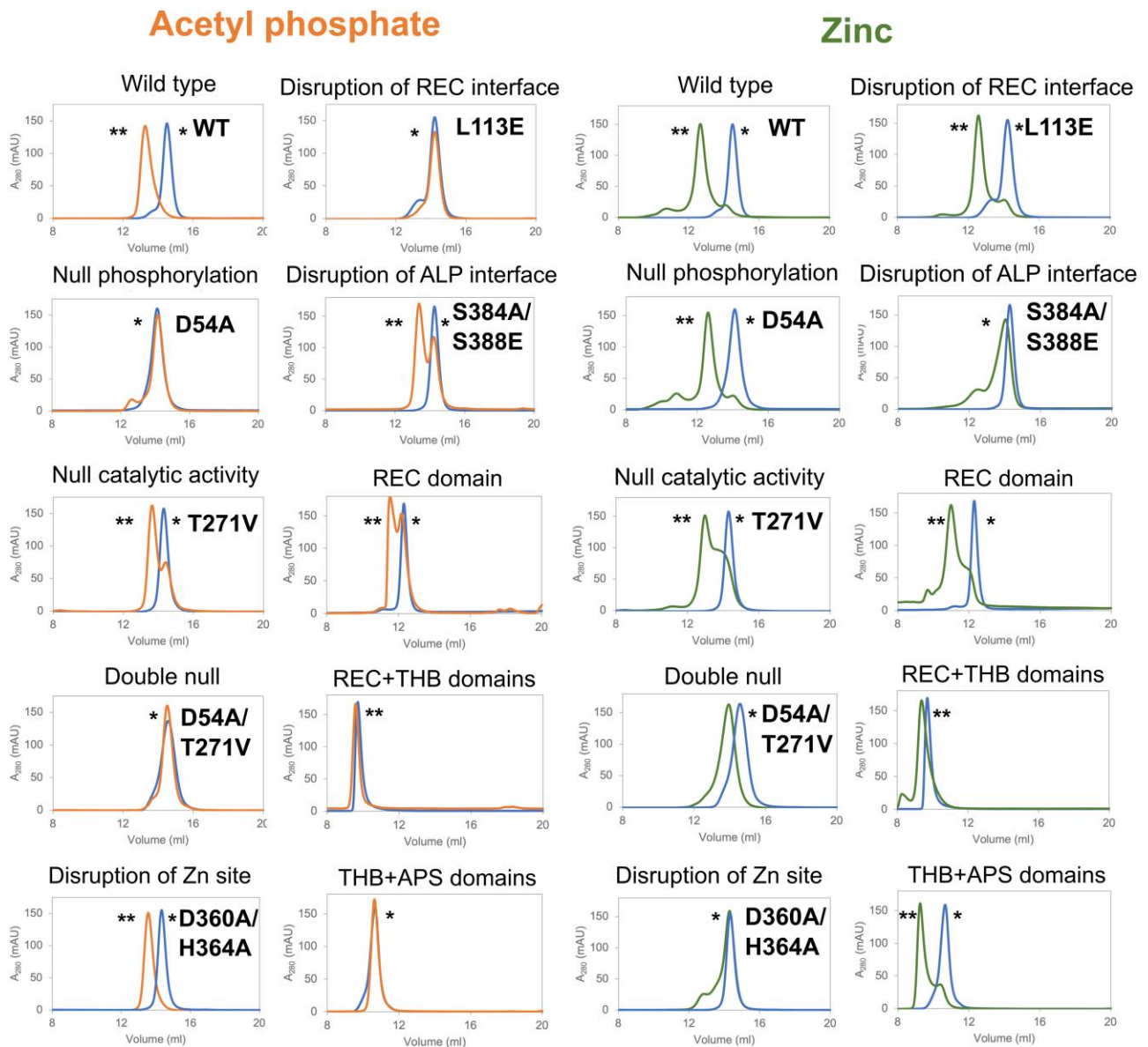
Fig. 5. *In vitro* dimerization of PorX$_{FJ}$ variants analyzed by size exclusion chromatography. PorX$_{FJ}$ proteins were incubated with acetyl phosphate in the presence of magnesium, or with zinc only. The blue, orange, and green chromatograms refer to the proteins in the absence of any dimerizing agent, proteins with AcP or Zn, respectively. The peaks representing the monomeric and dimeric states of the protein are labeled by (*) and (**), respectively. Wild-type and point mutation variants (~ 61 kDa) were analyzed by the Superdex200inc 10/300 GL column, while the truncation variants (REC domain: ~ 14 kDa, REC + THB domains: ~ 24 kDa and THB + APS domains: ~ 46 kDa) were analyzed by Superdex75inc 10/300 GL as per the column's ability to better separate proteins with lower molecular weights.

domains (PorX$_{PG}$ Δresidues 126–517), or the REC domain (PorX$_{PG}$ Δresidues 1–129) negatively affected the gingipain activity and thus indicating a reduced gingipains secretion by the T9SS (Fig. 6A). The reduced amidolytic activity observed suggests that the standalone domains cannot restore the entire T9SS function and associated virulence factors secretion in *P. gingivalis* and that all domains must be present to support downstream function (Fig. 6A). Next, we assessed the effect of key residues mutations, initially identified in PorX$_{FJ,}$ converted into their corresponding residues in PorX$_{PG}$. We utilized western blotting analyses (by anti-PorX$_{PG}$ antibody) to confirm that the expression levels of all these point mutation variants were similar to wild-type PorX$_{PG}$ and the effects seen are truly due to functional alteration (Fig. S10). Surprisingly, the gingipains amidolytic activities of the single phosphorylation-null and catalytically inactive variants (REC domain: D54A$_{FJ}$ to D58A$_{PG}$, or APS domain:

T271V$_{FJ}$ to T272V$_{PG}$) were only partially reduced when compared with the wild type (Kgp: REC-50% and APS-41%, Rgp: REC-61% and APS-67% of the wild type) (Fig. 6A). In contrast, the double null variant (D54A/T271V$_{FJ}$ to D58A/T272V$_{PG}$) had a more pronounced cumulative effect on gingipains secretion resulting in Kgp: 14% and Rgp: 25% of the wild type (Fig. 6A). Taken together, a clear indication of a cross talk between the REC domain and the APS domain can be seen. Additional analysis of mutants at the dimerization interface revealed that the REC domain dimerization interface (L113E$_{FJ}$ to L117E$_{PG}$) also resulted in reduced gingipain secretion (Kgp: 1% and Rgp: 2% of the wild type), while the APS domain dimerization interface (S384A/S388E$_{FJ}$ to S385A/S389E$_{PG}$) retaining the gingipains secretion and activity (Kgp: 70% and Rgp: 73% in of the wild type) (Fig. 6A). These results suggest that maintaining the dimerization ability of the REC domain, and not the APS domain, is of greater
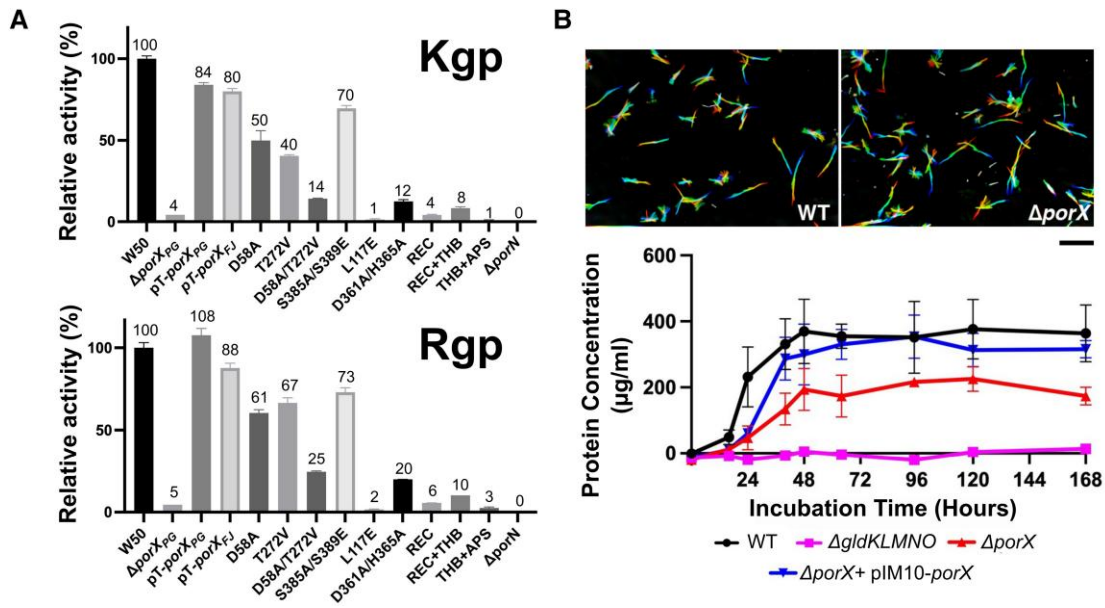
Fig. 6. *In vivo* characterization of PorX in *P. gingivalis* and *F. johnsoniae*. A) Gingipains enzymatic activity assay of *P. gingivalis* strain W50 containing different mutants of PorX. W50 and $\Delta porX_{PG}$ refer to wild type and PorX null mutant cells, respectively, both carrying empty pT-COW plasmids. The pT-*porX*$_{PG}$ and pT-*porX*$_{FJ}$ represent complementation of $\Delta porX_{PG}$ pT-COW cells with wild-type PorX$_{PG}$ and PorX$_{FJ}$, respectively. All other point mutations and truncations include the complementation of $\Delta porX_{PG}$ pT-COW cells with PorX$_{PG}$ carrying the relevant mutation. Experiments were performed in quadruplicates, and error bars indicate SDs. B) *Top*—Gliding motility assay for the wild-type and $\Delta porX$ null mutant in *F. johnsoniae*. A series of 180 frames were collected and colored from red (time zero) to yellow, green, cyan, and finally blue and then integrated into one image, resulting in rainbow traces of gliding cells. Scale bar at lower right indicates 20 μm and applies to all panels. *Bottom*—Growth curve of the wild type and $\Delta porX$ null mutant *F. johnsoniae* on a media containing chitin as the sole carbon source. Growth was presented as μg cellular protein/ml. Growth experiments were performed in triplicate, and error bars indicate SDs. The T9SS null mutant, $\Delta gldKLMNO$, that is unable to grow on chitin was used as the negative control. pIM10 contains the wild-type *porX*$_{FJ}$ and was used to complement the $\Delta porX$ mutant.

significance for the T9SS function. Although both the T272V$_{PG}$ catalytically inactive variant and the S385A/S389E$_{PG}$ APS dimerization interface variant maintained a significant secretion of gingipains, interfering with the Zn1 coordination site residues (D360A/H364A$_{FJ}$ to D361A/H365A$_{PG}$) resulted in reduced gingipain secretion (Kgp: 13% and Rgp: 20% of the wild type) (Fig. 6A). Based on the ICP-MS results for the D360A/H364A$_{FJ}$ double mutant, which revealed 0.63 zinc ions bound per monomer, it is evident that zinc coordination in Zn1 site has an additional stabilizing effect of on zinc coordination at Zn2 site, presenting with less than a single ion occupancy. Therefore, we conclude that zinc binding at the primary coordination site (Zn1) and associated conformational changes of the 358–369 residues stretch play a more substantial role in the function of the T9SS *in vivo* than the APS domain's ability to dimerize.

PorX$_{FJ}$ mediates digestive enzyme secretion in *F. johnsoniae* but not gliding motility

Deletion of the essential components of T9SS eliminates the crucial function associated with the T9SS, such as the ability to perform gliding motility and the secretion of digestive enzymes (13, 14, 61). Deletion of *porX* was previously conducted in *F. johnsoniae* strain CJ1827, a streptomycin-resistant *rpsL* mutant of UW101, and it was shown the deletion had no obvious effect on the motility and chitin utilization of *F. johnsoniae* (62). Here, we regenerated the *porX* deletion mutant in the wild-type strain UW101 and examined the phenotypes more quantitatively. First, we examined the *ΔporX* effect on the bacterium gliding motility via a classical motility assay and concluded that its genomic deletion does not impact the bacteria's ability to perform gliding motility (Fig. 6B). Next, we tested the *ΔporX* strain's ability to grow in a broth media

containing chitin as its primary carbon source. Under these restricted conditions, the bacteria must induce and secrete a major chitinase, ChiA, to allow bacterial growth. The dedicated chitinase is secreted by the T9SS and, therefore, serves as a marker for successful digestive enzyme secretion by the T9SS (19). While the deletion of the main T9SS rotary motor and trans-periplasmic complex ($\Delta gldKLMNO$) completely abolishes *F. johnsoniae*'s ability to grow on chitin, the deletion of *porX* results in ~40% reduced growth and total culture mass (Fig. 6B, lower panel). Overall, the cellular assays demonstrate that PorX does have a mild effect on the T9SS function in *F. johnsoniae*, particularly on the digestive enzyme secretion ability.

Discussion

Signal transduction by response regulators often requires the phosphorylation and subsequent dimerization of their REC domain (23). Here, we report on the structural determination of PorX, a noncanonical RR that comprises a classic REC domain and an additional enzymatic effector domain that exhibits phosphodiesterase activity.

PorX was crystallized in two distinct crystal forms, exhibiting an identical dimeric assembly in both asymmetric units. Therefore, the intertwined dimeric assembly is likely to represent a functional state. Structural analysis and subsequent co-crystallization experiments with phosphate analogs (such as BeF$_3$ or SO4^{2-}) established that the observed dimeric assembly represents the phosphorylated-like state and was further confirmed by the positioning of the REC domain's conserved TY residue pair. PorX's intertwined dimeric assembly gave rise not only to the classical dimeric interface between two REC domains, but also to an

Table 1. Summary table.

PorX$_{FJ}$	Dimerization		Phosphorylation		PDase activity	PorX$_{PG}$	Gingipains secretion
	AcP	Zn	REC	APS			
WT	+	+	+	+	+	WT	+++
D54A	−	+	−	+	+	D58A	++
T271V	+	+	+	−	−	T272V	++
L113E	−	+	+	+	+	L117E	+
D54A & T271V	−	+	−	−	−	D58A & T272V	+
D360A & H364A	+	−	+	−	−	D361A & H365A	+
S384A & S388E	+	−	+	+	−	S385A & S389E	+++
REC domain (1–121)	+	+	+	n/a	n/a	REC domain (1–125)	+
REC + THB domains (1–208)	(+)	(+)	+	n/a	n/a	REC + THB domains (1–207)	+
APS + THB domains (126–end)	−	+	n/a	+	+	APS + THB domains (130–end)	+

Results of the *in vitro* and *in vivo* characterization of PorX and its variants presented throughout the manuscript. *In vitro* characterization results include oligomeric state analyses by size exclusion chromatography, phosphorylation assays by intact protein MS analysis, and phosphodiesterase (PDase) assays. *In vivo* characterization results include the gingipain activity assays representing the T9SS's ability to secret gingipains in *P. gingivalis*. The symbols "+", "++", and "+++" in the gingipain secretion column represent average gingipain activities ranging from 0 to 33, 34 to 66, and 67 to 100%, respectively. The "n/a" indicates that phosphorylation could not be detected as the APS domain was truncated in this construct. The symbol "(+)" indicates that REC + THB domains truncated variant existed as a dimer even before the introduction of dimerizing agent.

additional interface between two APS domains with both interfaces sharing similar surface area dimensions. The recently determined crystallographic structure of PorX$_{PG}$ revealed a comparable monomeric fold and dimeric assembly to that of PorX$_{FJ}$ (Cα's RMSDs; monomer = 1.6 Å^2, dimer 1.9 Å^2), providing further evidence supporting our conclusion that the intertwined dimer reflects a functional state (Fig. S6) (30).

While the canonical response regulators typically require the phosphorylation of the conserved Asp residue (Asp54 in PorX$_{FJ}$) to induce dimerization of their REC domains, our findings demonstrate that zinc alone can trigger PorX's dimerization *in vitro*, even in the absence of a potent phosphodonor, like AcP (Fig. 5, Table 1). PorX can bind two zinc cations with high affinity as was demonstrated by biophysical measurements (ICP-MS and ITC). As such, we propose PorX may serve as a zinc sensor, such that altered zinc concentration could constitute one of the dimerization/activation signals for this regulatory cascade and the T9SS. It is important to note that the cellular zinc concentrations are tightly regulated. Studies measuring the total cellular zinc concentration in *E. coli* have demonstrated that the intracellular milieu consists of a myriad of tight zinc-binding proteins (fmol sensitivity), which greatly outnumber the full zinc ion content of the cell (up to 0.2 mM) (63). These findings suggested that under normal growth conditions, there is no persistent pool of free zinc in the cytoplasm (63). Similarly, mammalian cells maintain a total free zinc quota within a narrow range of ∼ 0.4 fmol/cell, corresponding to a total cellular zinc concentration in the millimolar range (64, 65). While the concentration of free zinc in *P. gingivalis*'s cytosol has yet to be experimentally determined, it is also likely to be low and tightly regulated. Under these conditions, PorX will not constantly exist as a dimer and it is plausible that changes in free zinc concentration trigger, or result from, the activation of the T9SS. Despite the observed nanomolar affinity, we cannot exclude the possibility that the zinc-induced dimerization might be specific to *in vitro* conditions.

PorX's effector domain adopts the fold of the APS. In support of its observed phosphodiesterase activity, the active site coordinates two zinc ions near the catalytic threonine residue. Structural comparison of the six monomers obtained from our two crystal forms revealed that residues 358–369, near the APS dimerization interface, are of flexible nature as they adopt multiple conformations. Notably, two crucial residues are found within the 358–369 residues stretch, namely Asp360 and His364, that are directly involved in zinc coordination at the APS domain. Therefore, alternation in the conformation of the 358–369 stretch can either establish or abolish the APS's Zn1 binding site and also affect the stabilization of the bound zinc in Zn2 site (Fig. 1C). Moreover, mutating the Asp360 and His364 dyad was found to affect the APS domain catalytic activity, zinc-induced dimerization and the overall T9SS function *in vivo* (Figs. 3 and 5, Table 1).

Although the role of the REC domain in signal transducing by response regulators has been previously established, the role of the APS effector domain *in vivo* remains unclear. Deletion of PorX$_{PG}$'s receiver or effector domains in *P. gingivalis* resulted in a significant decrease in gingipains secretion (< 10% of that observed for the wild type), underscoring the contribution of the individual domains to the regulation and function of the T9SS. While the intact APS domain evidently contributes to gingipain secretion, the T272V mutation, which impairs the domain's catalytic abilities, resulted in only a 50% decrease in gingipain secretion and activity levels, rather than a complete loss (Fig. 6A). Similarly, mutations at the conserved APS dimer interface (S385A/S389E) resulted in a retention of ∼ 71% of gingipain secretion (Fig. 6A). In contrast, these APS mutations, when tested *in vitro*, completely abolished phosphodiesterase activity

and significantly impaired zinc ion coordination (Figs. 3C and S5, Table 1). Notably, the D361A/H365A double mutation within the APS domain, which affects the Zn1 binding site coordination and is linked to the conformational changes of residues 358–369, was the only one to cause a significant loss of function both in vitro and a reduction in gingipain secretion *in vivo* (Fig. 1C, Table 1). Based on these findings, we conclude that while the enzymatic activity of APS is not essential for signal transduction and the function of the T9SS, the domain's structural integrity and particularly its zinc binding ability are of significant importance in *P. gingivalis*. Therefore, we propose that the region encompassing residues 358–369 along with its zinc-induced conformational alterations constitute a crucial regulatory site. This site is likely to mediate protein–protein interaction with one or more of the previously reported PorX interacting proteins, such as SigP, PorL, or another protein that must be identified. However, attempts to predict these suggested interactions particularly between PorX dimer, SigP or PorL by AlphaFold (66) did not yield reliable models, as the PorX dimer model always appears to adopt the helical conformation of residues 358–369.

The classical composition of response regulators' domains often includes an effector domain that directly interacts with DNA. In such cases, the phosphorylation of the REC domain triggers conformational changes, facilitating the effector domain's binding to DNA and, in particular, to promoter regions. Subsequently, promoter binding induces the transcription of specific gene(s) product(s) and triggers the desired cellular response. Previous biophysical studies report that to compensate for the lack of a DNA-binding effector domain and promote signal transduction throughout the cascade, $PorX_{PG}$ can bind and stabilize the transcription factor, SigP (24). Accordingly, it was shown that only SigP, and not PorX, can bind directly to promoter regions of T9SS-associated genes such as *porT*, *sov*, and *porP* and induce their transcription (24, 26). Other studies have challenged those findings and demonstrated that PorX can also directly bind to promoter regions of T9SS-associted genes, such as *sigP*, *porT*, *PGN_0341*, and *PGN_1639* (27). These findings supported the existence of a feedforward loop mechanism involving the direct interaction of both PorX and SigP with the T9SS-associated genes promoters (27). An additional study by the same group further suggested the THB linker domain to serve as the putative DNA-binding region (28). Here, our findings unambiguously demonstrate that PorX's effector domain folds and functions as a phosphodiesterase. Moreover, structural comparison and analysis of the entire structure and the THB domain, in particular, revealed no similarity to DNA-binding proteins or transcription factors. Accordingly, PorX's structure cannot shed light on the reported DNA-binding ability. We speculate that the attributed DNA-binding ability of PorX is mediated by an additional and yet-to-be-identified protein, likely to be involved in this regulatory cascade.

The orphan RR PorX was suggested to pair with the orphan SHK, PorY, to form a functional TCS (24, 26). While the genomic deletion of *porX* in *P. gingivalis* abolishes the T9SS function and renders the bacteria avirulent, the genomic deletion of *porY* does not (28, 59). As such, it is plausible that PorX might interact with other SHKs that exist in *P. gingivalis* to render its activity (28, 30, 67). An alternative activation mechanism might also rely on a yet-to-be-identified Asp-kinase or AcP in order to phosphorylate PorX's REC domain (30), similar to the observed effect of AcP in vitro (Figs. 4 and 5). Intriguingly, *in vivo* studies have shown that AcP phosphorylates and activates numerous orphan RR proteins (68). Although the exact concentration of AcP in *P. gingivalis* remains unknown, other bacteria such as *E. coli* have been found to contain at least 3 mM of AcP, which is sufficient for the effective autophosphorylation of RR proteins (69).

PorX is a highly conserved protein found in various bacterial species that utilize their T9SS. Accordingly, our findings demonstrate that $PorX_{FJ}$ can functionally complement the $\Delta porX_{PG}$ strain of *P. gingivalis*. While PorX plays a critical role in the function of the T9SS in the nongliding *P. gingivalis*, as evidenced by its effects on gingipains secretion and downstream T9SS-associated genes transcription (26–28, 30), its impact on the hallmark T9SS-associated functions in *F. johnsoniae* is different. Here, the deletion of the *porX* gene did not affect the bacteria's ability to perform gliding motility, suggesting that PorX does not regulate the T9SS-attributed gliding motility in *F. johnsoniae*. Next, we assessed the effect of *porX* deletion on the secretion of metabolic enzymes by the T9SS, specifically focusing on the chitinase ChiA. When grown on a chitin-only carbon-source media, the deletion of *porX* gene led to reduced growth compared to the wild type. However, in both gliding motility and chitinase growth assays, our control deletion of the T9SS-transperilapsmic rotary motor genes (*gldKLMNO*) completely abolished the gliding motility and the growth on chitin media, respectively. These findings suggest that while PorX is involved in the regulation of T9SS-associated functions in both *P. gingivalis* and *F. johnsoniae*, there are species-specific differences in its impact on the secretion of proteases and polysaccharide-degrading enzymes. Further investigation is needed to elucidate the precise mechanisms underlying these differences and the role of PorX in T9SS-related processes in different bacterial species.

Finally, it is important to note that the APS domain of PorX is conserved among T9SS-utilizing bacteria. This raises the possibility that the observed catalytic activity of PorX, in addition to its zinc-induced conformational changes, may have a significant role in the function of PorX in other Bacteroidetes species or in signaling pathways and cellular functions that are not directly related to the T9SS. A recent study has identified a cyclic di-adenosine monophosphate (c-di-AMP) signaling pathway in *P. gingivalis*, which is associated with bacterial growth, regulation of cell envelope homeostasis, and virulence (70). Considering that $PorX_{PG}$ was shown to hydrolyze pApA, a degradation product of c-di-AMP (30), it is plausible that PorX might participate in this signaling pathway. Further investigations are required to explore this possibility and unravel the precise involvement of PorX in other cellular processes and signaling pathways beyond the T9SS.

Acknowledgments

Supplementary Material

Supplementary material is available at *PNAS Nexus* online.

Funding

Author Contributions

A.S. and N.Z. initiated and designed the research project; A.S., H.M.K., I.M., M.A.H., J.F.T., Y.Z., M.E.D., and N.Z. performed research; Protein expression, purification, structure determination and biochemical assays by A.S. and N.Z, intact mass spectrometry was performed by M.A.H. and J.F.T, functional characterization in P. gingivalis by A.S., H.M.K., M.E.D. and N.Z, functional characterization in F. johnsoniae by I.M. And Y.Z. M.M. and J.P. contributed reagents to the study. A.S., H.M.K., I.M., M.A.H., C.S., M.M., J.P., M.S., J.F.T., Y.Z., M.E.D., and N.Z. analyzed the data. A.S., H.M.K., M.A.H., J.F.T., Y.Z., M.E.D. and N.Z. wrote the manuscript.

Preprints

This manuscript was posted on a preprint: https://doi.org/10.1101/2024.05.15.594396.

Data Availability

Atomic model and structure factors files have been deposited in the Protein Data Bank (PDB); accessions codes 8TEF, 8TED, 8TFF, 8TFM, and 8THP.

Change History

October 3, 2024: The Supplementary Material has been updated to remove author responses to reviewer comments, which had been erroneously included due to a vendor error.

References

1   Hajishengallis G, Diaz PI. 2020. *Porphyromonas gingivalis*: immune subversion activities and role in periodontal dysbiosis. *Curr Oral Health Rep*. 7:12–21.

2   Sedghi LM, Bacino M, Kapila YL. 2021. Periodontal disease: the good, the bad, and the unknown. *Front Cell Infect Microbiol*. 11:766944.

3   Könönen E, Gursoy M, Gursoy UK. 2019. Periodontitis: a multifaceted disease of tooth-supporting tissues. *J Clin Med*. 8:1135.

4   Kebschull M, Demmer RT, Papapanou PN. 2010. "Gum bug, leave my heart alone!"-epidemiologic and mechanistic evidence linking periodontal infections and atherosclerosis. *J Dent Res*. 89:879–902.

5   Benedyk M, *et al.* 2016. Gingipains: critical factors in the development of aspiration pneumonia caused by *Porphyromonas gingivalis*. *J Innate Immun*. 8:185–198.

6   Laugisch O, *et al.* 2016. Citrullination in the periodontium—a possible link between periodontitis and rheumatoid arthritis. *Clin Oral Investig*. 20:675–683.

7   Whitmore SE, Lamont RJ. 2014. Oral bacteria and cancer. *PLoS Pathog*. 10:e1003933.

8   Gao S, *et al.* 2016. Presence of *Porphyromonas gingivalis* in esophagus and its association with the clinicopathological characteristics and survival in patients with esophageal cancer. *Infect Agent Cancer*. 11:3.

9   Abbayya K, Puthanakar NY, Naduwinmani S, Chidambar YS. 2015. Association between periodontitis and Alzheimer's disease. *N Am J Med Sci*. 7:241–246.

10 Lasica AM, Ksiazek M, Madej M, Potempa J. 2017. The type IX secretion system (T9SS): highlights and recent insights into its structure and function. *Front Cell Infect Microbiol*. 7:215.

11 Li N, Collyer CA. 2011. Gingipains from *Porphyromonas gingivalis*—complex domain structures confer diverse functions. *Eur J Microbiol Immunol (Bp)*. 1:41–58.

12 Veith PD, Glew MD, Gorasia DG, Reynolds EC. 2017. Type IX secretion: the generation of bacterial cell surface coatings involved in virulence, gliding motility and the degradation of complex biopolymers. *Mol Microbiol*. 106:35–53.

13 Li N, *et al.* 2017. The type IX secretion system is required for virulence of the fish pathogen *Flavobacterium columnare*. *Appl Environ Microbiol*. 83:e01769-17.

14 Barbier P, *et al.* 2020. The type IX secretion system is required for virulence of the fish pathogen *Flavobacterium psychrophilum*. *Appl Environ Microbiol*. 86:1–22.

15 Good C, Davidson J, Wiens GD, Welch TJ, Summerfelt S. 2015. *Flavobacterium branchiophilum* and *F. succinicans* associated with bacterial gill disease in rainbow trout Oncorhynchus mykiss (Walbaum) in water recirculation aquaculture systems. *J Fish Dis*. 38:409–413.

16 Chen Z, *et al.* 2022. *Riemerella anatipestifer* T9SS effector SspA functions in bacterial virulence and defending natural host immunity. *Appl Environ Microbiol*. 88:e0240921.

17 Mark BM, Zhu Y. 2013. Gliding motility and por secretion system genes are widespread among members of the phylum bacteroidetes. *J Bacteriol*. 195:270–278.

18 Rhodes RG, Nelson SS, Pochiraju S, McBride MJ. 2011. *Flavobacterium johnsoniae* sprB is part of an operon spanning the additional gliding motility genes sprC, sprD, and sprF. *J Bacteriol*. 193:599–610.

19 Kharade SS, McBride MJ. 2015. *Flavobacterium johnsoniae* PorV is required for secretion of a subset of proteins targeted to the type IX secretion system. *J Bacteriol*. 197:147–158.

20 Kharade SS, McBride MJ. 2014. *Flavobacterium johnsoniae* chitinase ChiA is required for chitin utilization and is secreted by the type IX secretion system. *J Bacteriol*. 196:961–970.

21 Heath JE, *et al.* 2016. PG1058 is a novel multidomain protein component of the bacterial type IX secretion system. *PLoS One*. 11:e0164313.

22 Jacob-Dubuisson F, Mechaly A, Betton J-MM, Antoine R. 2018. Structural insights into the signalling mechanisms of two-component systems. *Nat Rev Microbiol.* 16:585–593.

23 Gao R, Bouillet S, Stock AM. 2019. Structural basis of response regulator function. *Annu Rev Microbiol.* 73:175–197.

24 Kadowaki T, *et al.* 2016. A two-component system regulates gene expression of the type IX secretion component proteins via an ECF sigma factor. *Sci Rep.* 6:23288.

25 Yukitake H, *et al.* 2020. Pora, a conserved C-terminal domain-containing protein, impacts the PorXY-SigP signaling of the type IX secretion system. *Sci Rep.* 10:21109.

26 Vincent MS, Durand E, Cascales E. 2016. The PorX response regulator of the *Porphyromonas gingivalis* PorXY two-component system does not directly regulate the type IX secretion genes but binds the PorL subunit. *Front Cell Infect Microbiol.* 6:96.

27 Jiang C, *et al.* 2021. A PorX/PorY and σ P feedforward regulatory loop controls gene expression essential for *Porphyromonas gingivalis* virulence. *mSphere.* 6:e0042821.

28 Yang D, Jiang C, Ning B, Kong W, Shi Y. 2021. The PorX/PorY system is a virulence factor of *Porphyromonas gingivalis* and mediates the activation of the type IX secretion system. *J Biol Chem.* 296:1–14.

29 Sato K, *et al.* 2010. A protein secretion system linked to bacteroidete gliding motility and pathogenesis. *Proc Natl Acad Sci U S A.* 107:276–281.

30 Schmitz C, *et al.* 2022. Response regulator PorX coordinates oligonucleotide signalling and gene expression to control the secretion of virulence factors. *Nucleic Acids Res.* 50:12558–12577.

31 Bond SR, Naus CC. 2012. RF-Cloning.org: an online tool for the design of restriction-free cloning projects. *Nucleic Acids Res.* 40: W209–W213.

32 Gibson DG, *et al.* 2009. Enzymatic assembly of DNA molecules up to several hundred kilobases. *Nat Methods.* 6:343–345.

33 Studier FW. 2005. Protein production by auto-induction in high-density shaking cultures. *Protein Expr Purif.* 41:207–234.

34 Saran A, Weerasinghe N, Thibodeaux CJ, Zeytuni N. 2022. Purification, crystallization and crystallographic analysis of the PorX response regulator associated with the type IX secretion system. *Acta Crystallogr F Struct Biol Commun.* 78:354–362.

35 Otwinowski Z, Minor W. 1997. Processing of X-ray diffraction data collected in oscillation mode. *Macromolecular Crystallography, Pt A.* 276:307–326.

36 Skubak P, *et al.* 2018. A new MR-SAD algorithm for the automatic building of protein models from low-resolution X-ray data and a poor starting model. *IUCrJ.* 5:166–171.

37 Emsley P, Lohkamp B, Scott WG, Cowtan K. 2010. Features and development of Coot. *Acta Crystallogr D Biol Crystallogr.* 66: 486–501.

38 McCoy AJ, *et al.* 2007. Phaser crystallographic software. *J Appl Crystallogr.* 40:658–674.

39 Murshudov GN, *et al.* 2011. REFMAC5 for the refinement of macromolecular crystal structures. *Acta Crystallogr D Biol Crystallogr.* 67: 355–367. https://doi.org/10.1107/S0907444911001314

40 Pettersen EF, *et al.* 2004. UCSF chimera—a visualization system for exploratory research and analysis. *J Comput Chem.* 25: 1605–1612.

41 Trempe JF, *et al.* 2016. Structural studies of the yeast DNA damage-inducible protein Ddi1 reveal domain architecture of this eukaryotic protein family. *Sci Rep.* 6:33671.

42 Rasool S, *et al.* 2022. Mechanism of PINK1 activation by autophosphorylation and insights into assembly on the TOM complex. *Mol Cell.* 82:44–59.e6.

43 Stevens MU, *et al.* 2023. Structure-based design and characterization of Parkin activating mutations. *Life Sci Alliance.* 6:e202201419.

44 Kim H-M, *et al.* 2021. A novel regulation of K-antigen capsule synthesis in *Porphyromonas gingivalis* is driven by the response regulator PG0720-directed antisense RNA. *Front Oral Health.* 2:701659.

45 Scott JC, Klein BA, Duran-Pinedo A, Hu L, Duncan MJ. 2013. A two-component system regulates hemin acquisition in *Porphyromonas gingivalis.* *PLoS One.* 8:e73351.

46 Potempa J, Nguyen KA. 2007. Purification and characterization of gingipains. *Curr Protoc Protein Sci.* Chapter 21:21.20.1–21.20.27.

47 Lasica AM, *et al.* 2016. Structural and functional probing of PorZ, an essential bacterial surface component of the type-IX secretion system of human oral-microbiomic *Porphyromonas gingivalis.* *Sci Rep.* 6:37708–37722.

48 Savchenko A, *et al.* 2003. Strategies for structural proteomics of prokaryotes: quantifying the advantages of studying orthologous proteins and of using both NMR and X-ray crystallography approaches. *Proteins.* 50:392–399.

49 Morita J, *et al.* 2016. Structure and biological function of ENPP6, a choline-specific glycerophosphodiester-phosphodiesterase. *Sci Rep.* 6:20995.

50 Lewis RJ, Brannigan JA, Muchová K, Barák I, Wilkinson AJ. 1999. Phosphorylated aspartate in the structure of a response regulator protein. *J Mol Biol.* 294:9–15.

51 Agarwal V, Borisova SA, Metcalf WW, van der Donk WA, Nair SK. 2011. Structural and mechanistic insights into C-P bond hydrolysis by phosphonoacetate hydrolase. *Chem Biol.* 18: 1230–1240.

52 Gorelik A, Liu F, Illes K, Nagar B. 2017. Crystal structure of the human alkaline sphingomyelinase provides insights into substrate recognition. *J Biol Chem.* 292:7087–7094.

53 Gorelik A, Randriamihaja A, Illes K, Nagar B. 2017. A key tyrosine substitution restricts nucleotide hydrolysis by the ectoenzyme NPP5. *FEBS J.* 284:3718–3726.

54 Albright RA, *et al.* 2014. Molecular basis of purinergic signal metabolism by ectonucleotide pyrophosphatase/phosphodiesterases 4 and 1 and implications in stroke. *J Biol Chem.* 289:3294–3306.

55 Gorelik A, Randriamihaja A, Illes K, Nagar B. 2018. Structural basis for nucleotide recognition by the ectoenzyme CD203c. *FEBS J.* 285:2481–2494.

56 Hausmann J, *et al.* 2011. Structural basis of substrate discrimination and integrin binding by autotaxin. *Nat Struct Mol Biol.* 18: 198–204.

57 Kato K, *et al.* 2012. Crystal structure of Enpp1, an extracellular glycoprotein involved in bone mineralization and insulin signaling. *Proc Natl Acad Sci U S A.* 109:16876–16881.

58 Zalatan JG, Zalatan JG, Fenn TD, Brunger AT, Herschlag D. 2006. Structural and functional comparisons of nucleotide pyrophosphatase/phosphodiesterase and alkaline phosphatase: implications for mechanism and evolution. *Biochemistry.* 45: 9788–9803.

59 Sato K, *et al.* 2010. A protein secretion system linked to bacteroidetes gliding motility and pathogenesis. *Proc Natl Acad Sci U S A.* 107:276–281.

60 Nonaka M, *et al.* 2014. Analysis of a Lys-specific serine endopeptidase secreted via the type IX secretion system in *Porphyromonas gingivalis.* *FEMS Microbiol Lett.* 354:60–68.

61 Zhu Y, McBride MJ. 2014. Deletion of the *Cytophaga hutchinsonii* type IX secretion system gene sprP results in defects in gliding motility and cellulose utilization. *Appl Microbiol Biotechnol.* 98: 763–775.

62 Shrivastava A, McBride MJ. 2013. Cell surface adhesins, exopolysaccharides and the Por (Type IX) secretion system of Flavobacterium johnsoniae [PhD Thesis]. Milwaukee (WI): University of Wisconsin-Milwaukee.

63 Outten CE, V O'Halloran T. 2001. Femtomolar sensitivity of metal-loregulatory proteins controlling zinc homeostasis. *Science*. 292: 2488–2492.

64 Suhy DA, Simon KD, Linzer DIH, O'Halloran TV. 1999. Metallothionein is part of a zinc-scavenging mechanism for cell survival under conditions of extreme zinc deprivation. *J Biol Chem*. 274:9183–9192.

65 Palmiter RD, Findley SD. 1995. Cloning and functional characterization of a mammalian zinc transporter that confers resistance to zinc. *EMBO J*. 14:639–649.

66 Jumper J, *et al*. 2021. Highly accurate protein structure prediction with AlphaFold. *Nature*. 596:583–589.

67 Mattos-Graner RO, Duncan MJ. 2017. Two-component signal transduction systems in oral bacteria. *J Oral Microbiol*. 9:1400858.

68 Wolfe AJ. 2010. Physiologically relevant small phosphodonors link metabolism to signal transduction. *Curr Opin Microbiol*. 13: 204–209.

69 Klein AH, Shulla A, Reimann SA, Keating DH, Wolfe AJ. 2007. The intracellular concentration of acetyl phosphate in *Escherichia coli* is sufficient for direct phosphorylation of two-component response regulators. *J Bacteriol*. 189: 5574–5581.

70 Moradali MF, *et al*. 2022. Atypical cyclic di-AMP signaling is essential for *Porphyromonas gingivalis* growth and regulation of cell envelope homeostasis and virulence. *NPJ Biofilms Microbiomes*. 8:53.